

Article

Phase Formation and Magnetic Properties of $(Y_{1-x}Sm_x)Co_5$ Melt-Spun Ribbons

Xiang Liu, Siyue Yang *, Xingping Zheng, Feilong Dai, Qingrong Yao and Jiang Wang * 

Guangxi Key Laboratory of Information Materials, School of Materials Science and Engineering, Guilin University of Electronic Technology, Guilin 541004, China; 13140580860@163.com (X.L.); zhengxingping579@163.com (X.Z.); dfldeyouxiang123@163.com (F.D.); qingry96@guet.edu.cn (Q.Y.)
* Correspondence: estelle210@163.com (S.Y.); waj124@guet.edu.cn (J.W.)

Abstract: Using X-ray diffraction (XRD) and a vibrating sample magnetometer (VSM), the effects of Sm substitution, wheel speed, and annealing temperature on the phase formation and magnetic properties of $(Y_{1-x}Sm_x)Co_5$ ($x = 0.2, 0.3, 0.4, 0.5$) melt-spun ribbons were investigated. The results indicate the following: (1) With the increase in Sm substitution, it was found that $(Y_{1-x}Sm_x)Co_5$ ribbons are entirely composed of the $(Y-Sm)Co_5$ phase with a $CaCu_5$ -type structure. Additionally, the coercivity gradually increases, while the remanence and saturation magnetization gradually decrease. (2) As the wheel speed increases, the $(Y_{1-x}Sm_x)Co_5$ ribbons exhibit an increasing proportion of $(Y-Sm)Co_5$ phase until reaching a speed of 40 m/s, where they are entirely composed of the $(Y-Sm)Co_5$ phase. Magnetic measurements show that the coercivity (H_{cj}) and remanence (B_r) of $(Y_{0.5}Sm_{0.5})Co_5$ ribbons increase gradually with increasing wheel speed, while saturation magnetization decreases. The variation in magnetic properties is mainly attributed to the formation of nucleation centers for reversed magnetic domain (2:7 and 2:17 phases); (3) $(Y_{0.5}Sm_{0.5})Co_5$ ribbons are composed of the $(Y-Sm)Co_5$ phase and a small amount of the Sm_2Co_7 phase after annealing at 550 °C, 600 °C, and 650 °C. Temperature elevation promotes crystallization of the amorphous phase, resulting in a gradual decrease in coercivity, while the remanence and saturation magnetization exhibit an overall increasing trend. Through continuous optimization of the process, favorable magnetic properties were achieved under the conditions of a 0.5 Sm substitution level, a wheel speed of 40 m/s, and an annealing temperature of 550 °C, with a coercivity of 7.98 kOe, remanence of 444 kA/m, and saturation magnetization of 508 kA/m.

Keywords: $SmCo_5$ ribbons; coercivity; remanent magnetization; heat treatment



Citation: Liu, X.; Yang, S.; Zheng, X.; Dai, F.; Yao, Q.; Wang, J. Phase Formation and Magnetic Properties of $(Y_{1-x}Sm_x)Co_5$ Melt-Spun Ribbons. *Metals* **2024**, *14*, 562. <https://doi.org/10.3390/met14050562>

Academic Editors: Aphrodite Ktena and Eric Hug

Received: 2 April 2024
Revised: 30 April 2024
Accepted: 7 May 2024
Published: 10 May 2024



Copyright: © 2024 by the authors. Licensee MDPI, Basel, Switzerland. This article is an open access article distributed under the terms and conditions of the Creative Commons Attribution (CC BY) license (<https://creativecommons.org/licenses/by/4.0/>).

1. Introduction

Nd-Fe-B permanent magnets are widely recognized for their exceptional magnetic properties at room temperature, making them indispensable in various modern industrial applications such as wind power generation and electric vehicles [1–4]. However, their utility is limited for high temperature applications due to their relatively low Curie temperature [5–8]. In contrast, $SmCo_5$ permanent magnets, as one of the most representative types among $RECo_5$ (where RE represents rare-earth elements) magnets, exhibit high thermal stability, meeting the stringent requirements of industrial applications. With a maximum operating temperature reaching up to 250 °C [9–12], $SmCo_5$ magnets ensure reliable performance even under elevated temperature conditions. Presently, various methods such as mechanical alloying, magnetron sputtering, and melt spinning are commonly employed for the preparation of $SmCo_5$ -based alloys [13–15]. For instance, Li et al. [13] utilized the melt spinning technique to successfully fabricate anisotropic nanocrystalline $SmCo_{4.8}Cr_{0.14}C_{0.08}$. They observed a transition in grain structure from randomly oriented equiaxed grains to dendritic morphology with increasing quenching speed. Remarkably, at a quenching speed of 50 m/s, the coercivity of the alloy reached 40.3 kOe, exhibiting excellent magnetic

properties. In other research, Su et al. [14] employed high-energy ball milling to prepare SmCo₅/α-Fe nanocomposite permanent magnetic materials. By subjecting the materials to heat treatment below 700 °C in a magnetic field, they successfully obtained nanocomposite magnets exhibiting strong soft-hard phase interactions, characterized by a single-phase hysteresis loop. Such distinctive microstructure and performance characteristics offer new insights and possibilities for the design and application of permanent magnetic materials. Recently, Gabay et al. [15] used another method to produce high-coercivity YCo₅ and SmCo₅ powders by employing a mechanosynthesis approach based on conventional powder grinding. They employed mechanical activation using a mixture of rare earth oxides with Co, Ga, and CaO, followed by short-term annealing and washing/separation processes to produce high-coercivity YCo₅ and SmCo₅ powders. They found out that the hard magnetic properties of YCo₅ powders synthesized via mechanosynthesis are comparable to those of conventionally prepared SmCo₅ powders, offering a novel avenue for the controllable synthesis of permanent magnetic materials.

The elements lanthanum (La), cerium (Ce), and yttrium (Y), which are found abundantly in rare-earth resources, are capable of forming a 1:5 phase with the transition metal cobalt (Co). Compounds such as LaCo₅, CeCo₅, and YCo₅, as well as SmCo₅, all crystallize into the hexagonal CaCu₅-type crystal structure, characterized by a space group of P6/mmm. However, it is noteworthy that only YCo₅ exhibits intrinsic magnetic properties that are on par with or even surpass those of SmCo₅ [16–19]. Specifically, both SmCo₅ and YCo₅ exhibit high magnetic anisotropy, owing to the interaction between the 4f electrons of samarium (Sm) atoms and the hexagonal crystal field, as well as the spin-orbit coupling of the 3d electrons of cobalt (Co) atoms [20]. This interplay of electronic configurations contributes significantly to the magnetocrystalline anisotropy observed in these materials. Considering Y as a high-abundance rare-earth element, it is believed that adding the element Y is a promising and cost-effective way to enhance the magnetic properties of 1:5-type permanent magnets [21–23].

Research on SmCo₅ and YCo₅ in the past has mainly focused on investigating the incorporation of various elements into their structures. These elements are the transition metals, like Fe, Cu, Ti, Zr, Ni, and Mn [24–30], non-metallic elements, such as C, H, and Si [31–33], and rare-earth elements, like La, Ce, Pr, Nd, Dy, and Tm [34–38]. The aim has been to fine-tune the phase composition and magnetic characteristics of permanent magnets. For instance, Larson et al. [25] investigated the impact of Fe doping on the magnetic anisotropy of SmCo₅ and YCo₅, employing both experimental and computational techniques. They observed that when the doping level of Fe was approximately 3–4% in SmCo_{5-x}Fe_x and 6–7% in YCo_{5-x}Fe_x, the magneto-crystalline anisotropy energy (MAE) increased by about 1 meV/f.u. However, with further increases in Fe doping, the magnetic anisotropy rapidly declined. This phenomenon was also observed in other RECo_{5-x}Fe_x magnets. Chen et al. [34], on the other hand, systematically investigated the phase structures and magnetic properties of Sm_{1-x}La_xCo₅ and Sm_{1-x}Ce_xCo₅ alloys tuning La and Ce doping levels and annealing conditions. Their findings indicated a superior magnetic performance in La-doped SmCo₅ compared to Ce-doped counterparts. Additionally, Banerjee et al. [37] investigated the structural and magnetization characteristics of Dy_{1-x}Y_xCo₅ compounds, finding an enhancement in the axial magneto-crystalline anisotropy energy (MAE) with increasing Y content. Despite these efforts, research on the phase evolution, microstructural intricacies, and magnetic behaviors of (Y_{1-x}Sm_x)Co₅ alloys still needs research. Passos et al. [20] conducted an investigation on the effect of substituting Y with Sm on the magnetic properties of (Y_{1-x}Sm_x)Co₅ (x = 0.0, 0.1, 0.2, 0.3, and 0.4) alloys. Furthermore, Gonzalez et al. [39] reported a coercivity of 12 kOe for Y_{0.5}Sm_{0.5}Co₅ melt-spun ribbon at a wheel speed of 40 m/s. In order to deeply study the relationship between the composition, phase formation, preparation conditions, and magnetic properties of rare-earth element Sm and YCo₅ alloys, (Y_{1-x}Sm_x)Co₅ alloys were prepared using melt spinning technology. The phase formation and magnetic properties of these alloys were analyzed. The effects of Sm

substitution, wheel speeds, and annealing temperatures under different conditions on the magnetic properties of $(Y_{1-x}Sm_x)Co_5$ ribbons were investigated.

2. Experiment

The $(Y_{1-x}Sm_x)Co_5$ ($x = 0.2, 0.3, 0.4, 0.5$) alloys were synthesized with the arc-melting method, using high-purity bulk metals Y, Sm, and Co (99.99% purity) as raw materials. Due to the high volatility of the rare-earth elements Y and Sm at high temperatures, an additional 5% of Y and Sm was added during weighing to compensate for evaporation. To ensure compositional homogeneity, the alloys underwent four re-melting cycles during the arc-melting process. Subsequently, the alloys were crushed into small pieces (approximately 2.5 g) and loaded into a quartz tube with an orifice (diameter approximately 0.9 mm). They were then spun onto a copper wheel in an argon atmosphere at various wheel speeds (20–40 m/s) to produce melt-spun ribbons. Subsequently, the melt-spun ribbons were placed in quartz tubes filled with argon, annealed at different temperatures (500–650 °C) for 30 min, and then quenched in ice water. The width of the melt-spun ribbons ranged from about 8 to 13 mm, and the thickness was approximately 2 to 3 mm.

The $(Y_{1-x}Sm_x)Co_5$ melt-spun ribbons (about 0.5 g) were placed in an agate mortar filled with anhydrous ethanol to prevent oxidation and then were manually grinded into powders, which was sieved to achieve a particle size of 250 mesh. XRD measurements of powders were performed on a PLXcel 3D X-ray diffractometer (Tokyo, Japan) in the range 20–70° at 45 kV and 25 mA using a Co K radiation source. The crystal structure of the $(Y_{1-x}Sm_x)Co_5$ ribbons was determined by analyzing XRD patterns. The magnetic properties of the melt-spun ribbons were measured at room temperature using a vibrating sample magnetometer (VSM, Lakeshore Model 7400 740H, Carson, CA, USA). The demagnetization correction of the melt-spun ribbons was neglected because the applied external field is parallel to the plane of the ribbons during the magnetic measurements.

3. Results and Discussion

3.1. Structure and Magnetic Properties of $(Y_{1-x}Sm_x)Co_5$ Ribbons

Figure 1 shows the XRD spectra of the $(Y_{1-x}Sm_x)Co_5$ ($x = 0.2, 0.3, 0.4, 0.5$) melt-spun ribbons at a wheel speed of 40 m/s. In Figure 1a, it is observed that the $(Y_{1-x}Sm_x)Co_5$ ribbons contain a continuous solid solution phase $(Y-Sm)Co_5$, exhibiting a $CaCu_5$ -type structure with a space group of $P63/mmc$, as identified by comparison with standard PDF cards. Figure 1b presents the local XRD spectra of these ribbons in the 40° to 45° range, revealing a leftward shift of the diffraction peaks of the $(Y-Sm)Co_5$ phase with increasing Sm atomic substitution. This shift is attributed to the larger atomic radius of Sm compared to Y, leading to a decrease in diffraction angle according to the Bragg equation. Figure 2 displays the variations in lattice parameters and unit cell volumes of the $(Y-Sm)Co_5$ phase as the Sm atomic substitution increases. Specific numerical values are provided in Table 1. It is observed from Figure 2 that the lattice parameter 'a' and cell volume of the $(Y-Sm)Co_5$ phase slightly increase with increasing Sm substitution, while the lattice parameter 'c' gradually decreases. This trend may be attributed to the lattice constants of $SmCo_5$ phase, where 'a' = 4.998 (Å) is greater than that of YCo_5 phase with 'a' = 4.928 (Å), while 'c' = 3.976 (Å) for $SmCo_5$ is smaller than 'c' = 3.992 (Å) for YCo_5 [40,41].

Figure 3 depicts the initial magnetization curves and hysteresis loops (M-H curves) of the $(Y_{1-x}Sm_x)Co_5$ ($x = 0.2, 0.3, 0.4, 0.5$) melt-spun ribbons prepared at a wheel speed of 40 m/s. Figure 4 illustrates the variations in remanence (B_r), coercivity (H_{c1}), and saturation magnetization (M_s) of the $(Y_{1-x}Sm_x)Co_5$ ($x = 0.2, 0.3, 0.4, 0.5$) melt-spun ribbons with the substitution of Sm. The corresponding magnetic parameters are listed in Table 1. From Figure 3a, it can be observed that the initial magnetization curve of the $(Y_{1-x}Sm_x)Co_5$ melt-spun ribbons shows a rapid increase in magnetization intensity at low magnetic fields. As the magnetic field intensity increases, the magnetization intensity tends to saturate, indicating that the magnetization mechanism is regulated by the nucleation field [42]. From Table 1 and Figure 4, it is evident that the saturation magnetization of the $(Y_{1-x}Sm_x)Co_5$

melt-spun ribbons decreases from 726 kA/m to 488 kA/m with increasing Sm substitution. Due to the higher saturation magnetization of YCo_5 compared to SmCo_5 , the increase in Sm content promotes the formation of SmCo_5 in the continuous solid solution phase $(\text{Y-Sm})\text{Co}_5$, reducing the YCo_5 content and consequently leading to a decrease in the saturation magnetization of the ribbon [43,44]. Figure 3b shows the hysteresis loops of the $(\text{Y}_{1-x}\text{Sm}_x)\text{Co}_5$ melt-spun ribbons, indicating that the coercivity increases from 0.79 to 7.98 kOe with the increasing substitution of Sm. This significant enhancement is attributed to the introduction of Sm, which also leads to an increase in the proportion of SmCo_5 in the continuous solid solution phase $(\text{Y-Sm})\text{Co}_5$. Compared to YCo_5 , SmCo_5 exhibits higher coercivity, thus the coercivity of the ribbon increases with increasing Sm content. Meanwhile, the remanence decreases from 479 kA/m to 406 kA/m, exhibiting a trend similar to the decrease in saturation magnetization, both attributed to the increase in the volume fraction of SmCo_5 in the continuous solid solution phase $(\text{Y-Sm})\text{Co}_5$.

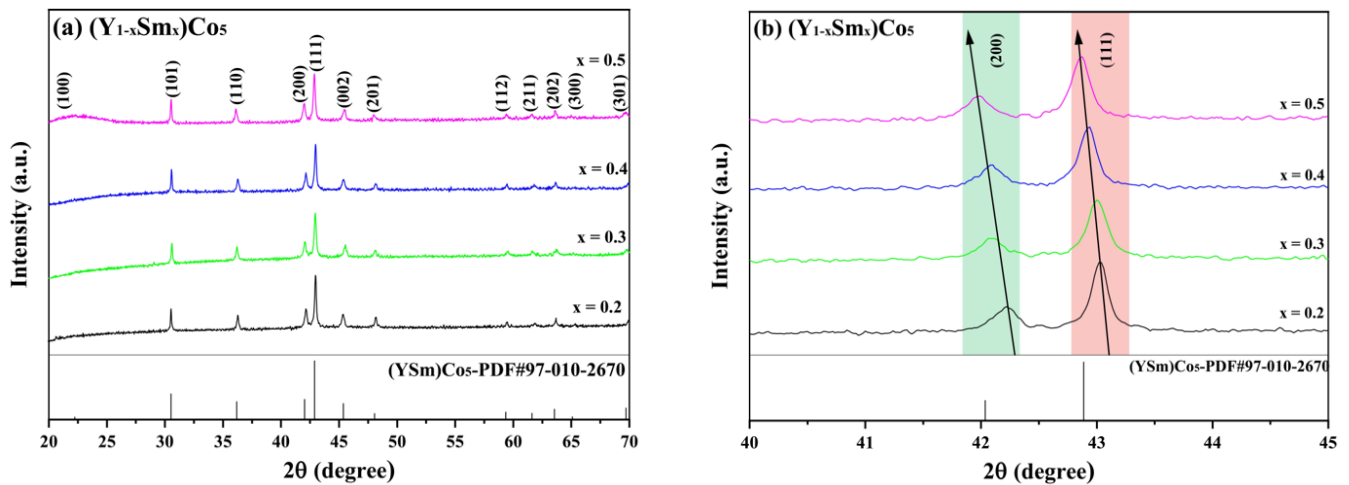


Figure 1. XRD patterns (a) and local XRD patterns (b) of $(\text{Y}_{1-x}\text{Sm}_x)\text{Co}_5$ ($x = 0.2, 0.3, 0.4, 0.5$) melt-spun ribbons prepared at a wheel speed of 40 m/s. The arrows in panel (b) indicate the direction of diffraction peak shifts.

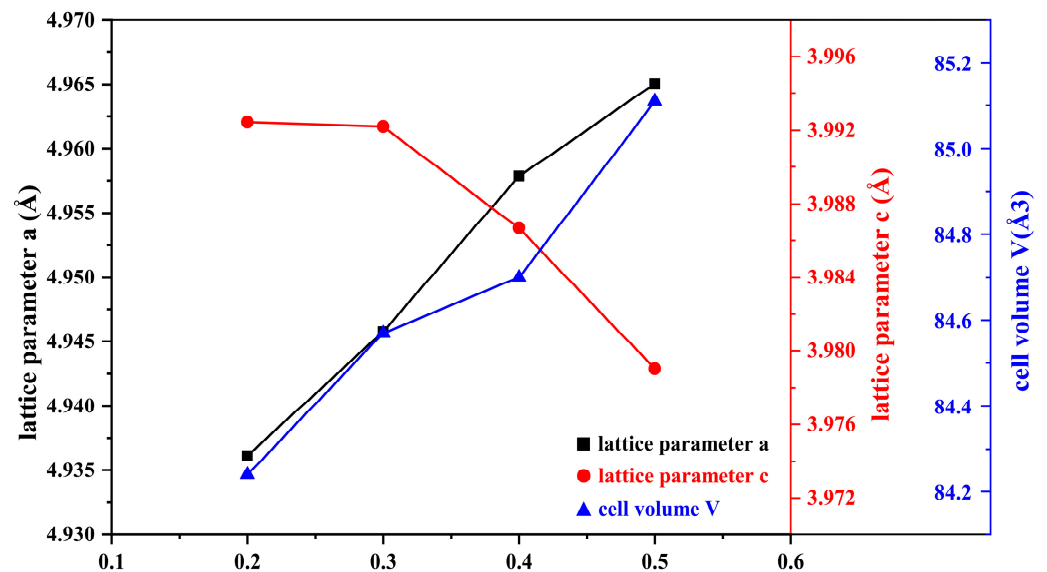
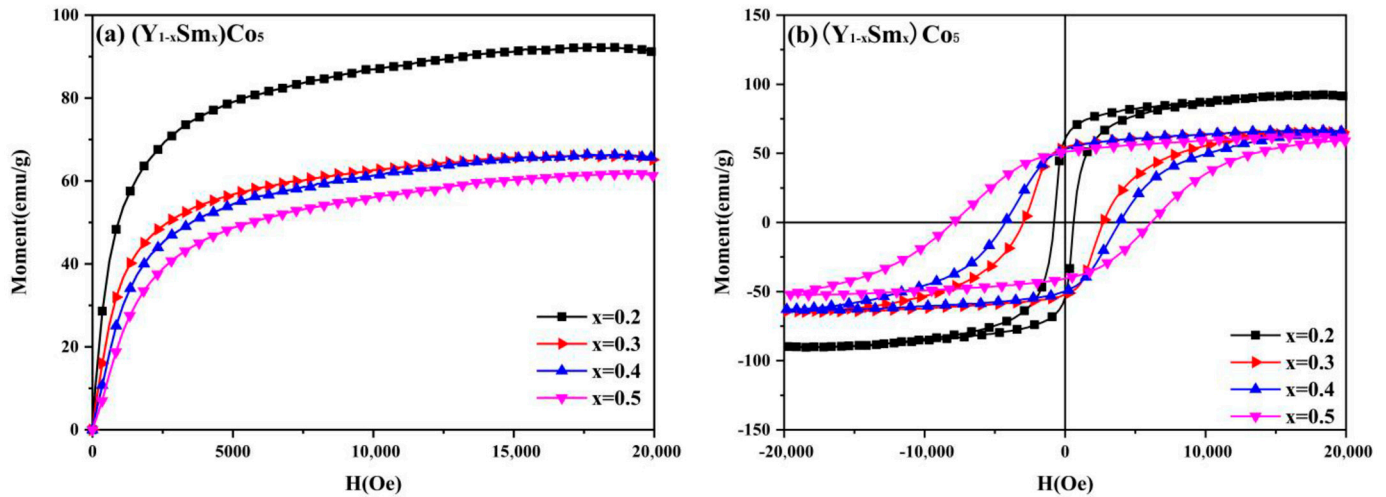
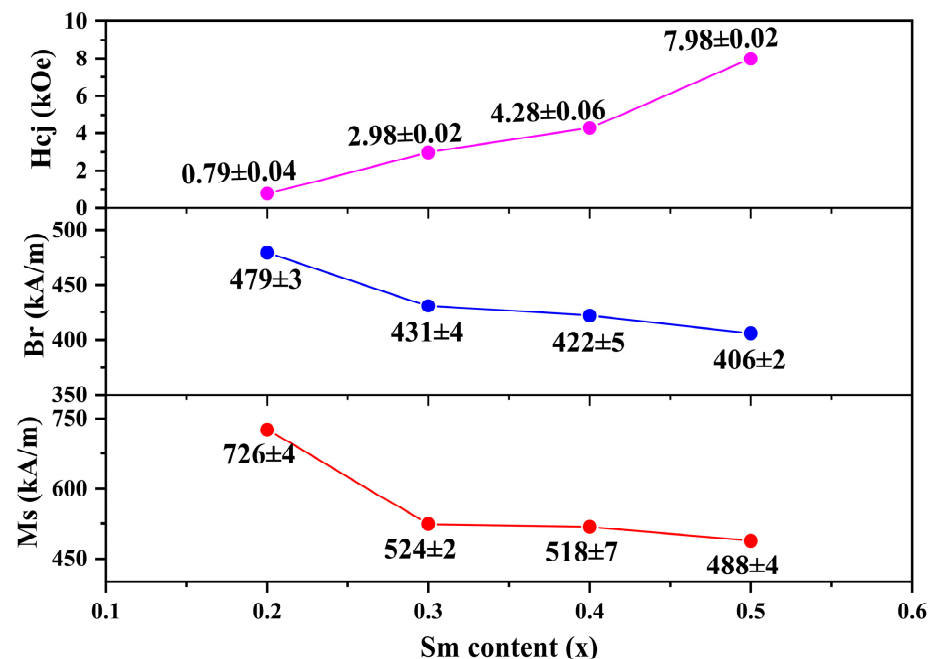


Figure 2. Lattice parameters and cell volumes of $(\text{Y-Sm})\text{Co}_5$ phase in $(\text{Y}_{1-x}\text{Sm}_x)\text{Co}_5$ ($x = 0.2, 0.3, 0.4, 0.5$) melt-spun ribbons.

Table 1. Lattice parameters and cell volumes of $(Y_{1-x}Sm_x)Co_5$ phase and magnetic properties in $(Y_{1-x}Sm_x)Co_5$ melt-spun ribbons.

$(Y_{1-x}Sm_x)Co_5$ Ribbons	Lattice Parameters			Cell Volumes (\AA^3)	Magnetic Properties		
	a (\AA)	c (\AA)	c/a		H_{cj} (kOe)	B_r (kA/m)	M_s (kA/m)
x = 0.2	4.9361(1)	3.9924(6)	0.8088	84.24(5)	0.79 ± 0.04	479 ± 3	726 ± 4
x = 0.3	4.9457(1)	3.9922(6)	0.8072	84.57(6)	2.98 ± 0.02	431 ± 4	524 ± 2
x = 0.4	4.9578(1)	3.9866(6)	0.8041	84.70(6)	4.28 ± 0.06	422 ± 5	518 ± 7
x = 0.5	4.9650(1)	3.9790(6)	0.8014	85.11(7)	7.98 ± 0.02	406 ± 2	488 ± 4

**Figure 3.** Initial magnetization curves (a) and hysteresis loops (b) of $(Y_{1-x}Sm_x)Co_5$ ($x = 0.2, 0.3, 0.4, 0.5$) melt-spun ribbons.**Figure 4.** Magnetic properties (H_{cj} , B_r and M_s) of $(Y_{1-x}Sm_x)Co_5$ ($x = 0.2, 0.3, 0.4, 0.5$) melt-spun ribbons as a function of Sm substitution.

In this section, an investigation was conducted into the phase structure, phase composition, and magnetic properties of $(Y_{1-x}Sm_x)Co_5$ ($x = 0.2, 0.3, 0.4, 0.5$) melt-spun ribbons at a wheel speed of 40 m/s. It was confirmed that the $(Y_{1-x}Sm_x)Co_5$ ribbons exhibit a $CaCu_5$ -

type structure, with the XRD diffraction peaks shifting to the left as the substitution amount of Sm increases. The lattice parameter 'a' and the unit cell volume of the (Y-Sm)Co₅ phase showed a slight increase, while the lattice parameter 'c' gradually decreased. Magnetic measurement results indicated that the magnetization mechanism is regulated by the nucleation field. With an increase in the substitution amount of Sm, the saturation magnetization of the (Y_{1-x}Sm_x)Co₅ ribbons decreased from 726 kA/m to 488 kA/m, coercivity increased from 0.79 kOe to 7.98 kOe, and remanence decreased from 479 kA/m to 406 kA/m. These changes were attributed to the increase in the proportion of SmCo₅ in the continuous solid solution phase (Y-Sm)Co₅.

3.2. Structural and Magnetic Properties of (Y_{0.5}Sm_{0.5})Co₅ Ribbons at Different Wheel Speeds

In the previous section, an investigation on the structure and magnetic properties of (Y_{1-x}Sm_x)Co₅ (x = 0.2, 0.3, 0.4, 0.5) melt-spun ribbons prepared at a wheel speed of 40 m/s revealed that at a Sm substitution level of 0.5, i.e., x = 0.5, the ribbons exhibited a higher coercivity of 7.98 kOe. In order to further investigate the structural and magnetic property variations in (Y_{1-x}Sm_x)Co₅ melt-spun ribbons under different conditions, we kept x = 0.5 constant and varied the wheel speed. (Y_{0.5}Sm_{0.5})Co₅ melt-spun ribbons were prepared at different wheel speeds (20 m/s, 30 m/s, 40 m/s) to examine their structural and magnetic property changes.

Figure 5 shows the X-ray diffraction (XRD) patterns of the (Y_{0.5}Sm_{0.5})Co₅ melt-spun ribbons prepared at different wheel speeds (20 m/s, 30 m/s, 40 m/s). It can be observed from Figure 5 that at a wheel speed of 20 m/s, the melt-spun ribbon consists entirely of the (Y-Sm)₂Co₁₇ phase; at 30 m/s, the ribbon comprises small amounts of the Sm₂Co₇ and (Y-Sm)Co₅ phases, while at 40 m/s, the ribbon consists entirely of the (Y-Sm)Co₅ phase. During the preparation of the melt-spun ribbons, slower wheel speeds lead to the accumulation of molten metal on the surface of the copper roller, resulting in thicker ribbon layers and slower cooling rates. According to the Y-Co [45] and Sm-Co [46] binary phase diagrams, the 1:5 phase decomposes into 2:7 and 2:17 phases at low temperatures. Thus, at a wheel speed of 20 m/s, the decomposition of (Y-Sm)Co₅ phase forms the (Y-Sm)₂Co₁₇ phase, while at 30 m/s, partial decomposition of (Y-Sm)Co₅ phase forms Sm₂Co₇ phase. However, at a wheel speed of 40 m/s, the resulting ribbon has a thinner layer and faster cooling rate, preventing the (Y-Sm)Co₅ phase from undergoing a phase transformation. When the speed is 40 m/s, there is an unclear diffraction peak between 20° and 25° in the diffraction pattern, indicating the presence of an amorphous phase in the (Y_{0.5}Sm_{0.5})Co₅ melt-spun ribbon at this speed. To further confirm the existence of the amorphous phase, we calculated the crystallinities at wheel speeds of 20 m/s, 30 m/s, and 40 m/s, which were found to be 60.4%, 53.2%, and 45.7%, respectively. The formation of the amorphous phase is attributed to the higher wheel speed accelerating the cooling rate, resulting in partial solidification of the alloy melt before crystallization.

Figure 6 depicts the initial magnetization curves and hysteresis loops (M-H curves) of (Y_{0.5}Sm_{0.5})Co₅ melt-spun ribbons at different wheel speeds. Figure 7 shows the variations in remanence (B_r), coercivity (H_{cj}), and saturation magnetization (M_s) with Sm substitution for the (Y_{0.5}Sm_{0.5})Co₅ melt-spun ribbons, with corresponding magnetic parameters presented in Table 2. In Figure 6a, it can be observed that the initial magnetization intensity of the (Y_{0.5}Sm_{0.5})Co₅ melt-spun ribbon increases with the increasing applied magnetic field, gradually approaching saturation, with the magnetization mechanism being regulated by the nucleation field. From Table 2 and Figure 7, it can be seen that with increasing wheel speed, the saturation magnetization of the (Y_{0.5}Sm_{0.5})Co₅ melt-spun ribbon decreases from 870 kA/m to 488 kA/m. Consistent with previous research findings, the reduction in saturation magnetization intensity is attributed to the gradual decrease in crystallinity as the wheel speed increases in the (Y_{0.5}Sm_{0.5})Co₅ melt-spun ribbon, indicating an increasing proportion of the amorphous phase. Materials with non-crystalline structure exhibit higher magnetic hysteresis losses, resulting in increased energy dissipation during magnetization and consequently lowering the saturation magnetization. Additionally, amorphous struc-

tures typically lack distinct magnetic domain structures, resulting in higher domain wall energies, thus increasing the energy cost for magnetic moment reversal and decreasing the magnetization intensity. Figure 6b presents the hysteresis loop of the $(Y_{0.5}Sm_{0.5})Co_5$ melt-spun ribbons. From Figures 6b and 7, it can be seen that with increasing wheel speed, the coercivity of the $(Y_{1-x}Sm_x)Co_5$ melt-spun ribbon increases from 0.4 to 7.98 kOe. This is attributed to the gradual increase in the proportion of the 1:5 phase with high coercivity as the speed increases. Additionally, when the wheel speed is 20 m/s, the ribbon is composed entirely of the $(Y-Sm)_2Co_{17}$ phase, which is a soft magnetic phase with lower coercivity. However, as the wheel speed increases to 30 m/s, the ribbon consists of Sm_2Co_7 and $(Y-Sm)Co_5$, with the 2:7 phase becoming the nucleation center for demagnetization within the ribbon, resulting in lower coercivity compared to when the speed is 40 m/s. At a wheel speed of 40 m/s, both coercivity and remanence significantly increase, indicating a notable enhancement in remanence effect, primarily attributed to the reduction in the 2:7 and 2:17 phases, which reduces the nucleation centers for demagnetization.

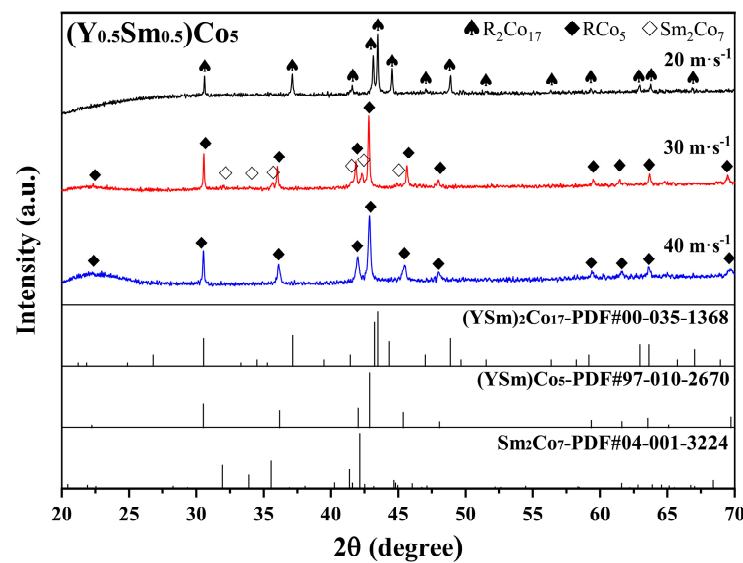


Figure 5. XRD patterns of $(Y_{0.5}Sm_{0.5})Co_5$ as-cast ribbons prepared at wheel speeds of 20 m/s, 30 m/s and 40 m/s.

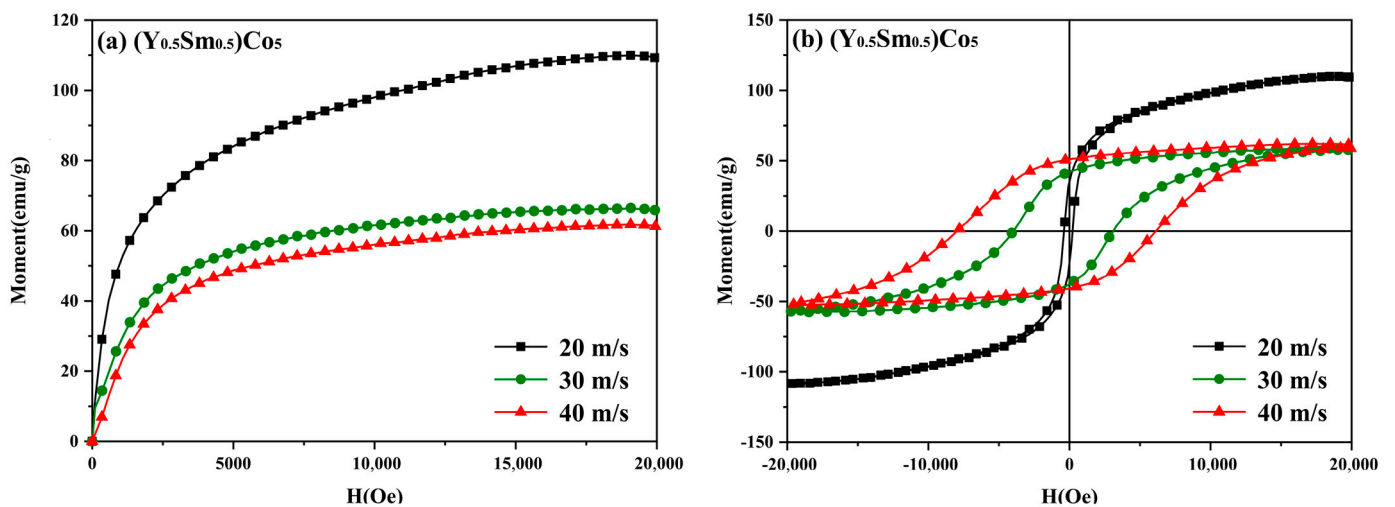


Figure 6. Initial magnetization curves (a) and hysteresis loops (b) of $(Y_{0.5}Sm_{0.5})Co_5$ ribbon prepared at different wheel speeds.

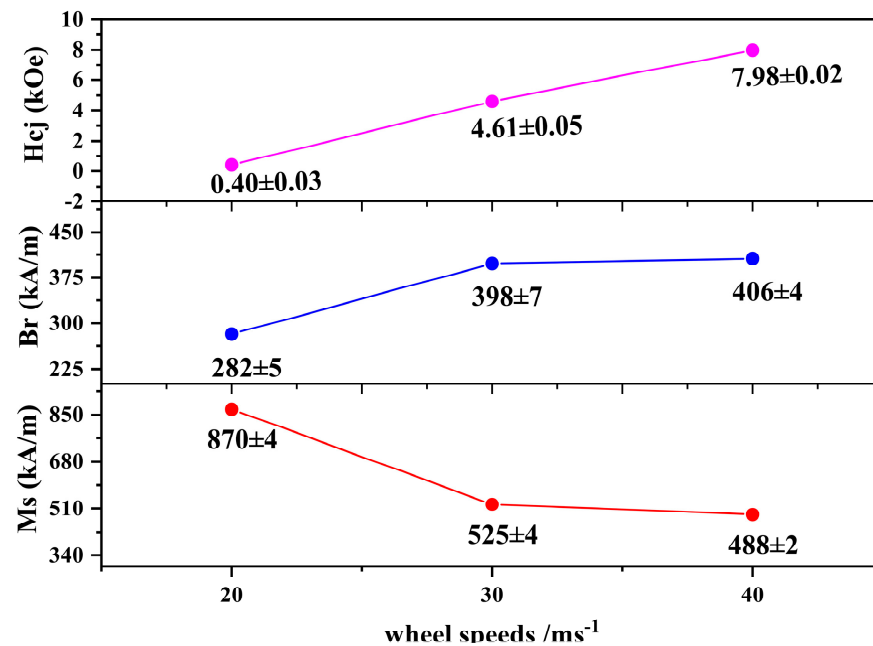


Figure 7. Magnetic properties (H_{cj} , B_r , and M_s) of $(Y_{0.5}Sm_{0.5})Co_5$ melt-spun ribbons as a function of wheel speeds.

Table 2. Magnetic properties of $(Y_{0.5}Sm_{0.5})Co_5$ ribbons prepared at different wheel speeds and annealed at different temperatures for 30 min.

Wheel Speed (m/s)	Annealed Temperature ($^{\circ}C$)	H_{cj} (kOe)	B_r (kA/m)	M_s (kA/m)
20		0.40 ± 0.03	282 ± 5	870 ± 4
30	no annealed	4.61 ± 0.05	398 ± 7	525 ± 4
40	no annealed	7.98 ± 0.02	406 ± 4	488 ± 2
40	550	7.98 ± 0.05	444 ± 3	502 ± 3
	600	6.96 ± 0.07	376 ± 3	479 ± 6
	650	5.17 ± 0.02	463 ± 5	548 ± 5

In this section, we investigated the phase structure, phase composition, and magnetic properties of $(Y_{0.5}Sm_{0.5})Co_5$ melt-spun ribbons prepared at different wheel speeds (20 m/s, 30 m/s, 40 m/s). It was found that at a wheel speed of 20 m/s, the ribbons were composed of the $(Y-Sm)_2Co_{17}$ phase; at 30 m/s, they contained small amounts of Sm_2Co_7 and $(Y-Sm)Co_5$, while at 40 m/s, the ribbons were entirely composed of the $(Y-Sm)Co_5$ phase. Magnetic measurement results revealed that with increasing wheel speed, the saturation magnetization of the $(Y_{0.5}Sm_{0.5})Co_5$ melt-spun ribbons decreased from 870 kA/m to 488 kA/m. This decrease in saturation magnetization was attributed to the increase in the amorphous phase. Meanwhile, the remanence and coercivity increased with increasing speed, primarily due to the reduction in the 2:7 and 2:17 phases, thereby lowering the demagnetization nucleation centers.

3.3. Structure and Magnetic Properties of $(Y_{0.5}Sm_{0.5})Co_5$ Ribbons Annealed at Different Temperatures

In the previous sections, investigations were carried out on the structure and magnetic properties of $(Y_{1-x}Sm_x)Co_5$ ($x = 0.2, 0.3, 0.4, 0.5$) melt-spun ribbons prepared with different Sm substitutions and wheel speeds. It was found that when the Sm substitution is 0.5 and the wheel speed is 40 m/s, the melt-spun ribbon exhibits optimal magnetic properties. In order to further explore the structural and magnetic property changes of the $(Y_{0.5}Sm_{0.5})Co_5$ melt-spun ribbons under different conditions, in this section, ribbons

prepared at a wheel speed of 40 m/s will be subjected to heat treatment at different temperatures (550 °C, 600 °C, and 650 °C). This aims to further investigate the variations in structure and magnetic properties.

Figure 8 displays the X-ray diffraction (XRD) patterns of $(Y_{0.5}Sm_{0.5})Co_5$ ribbons annealed at various temperatures for 30 min, prepared with a wheel speed of 40 m/s. It can be observed from Figure 8 that the $(Y_{0.5}Sm_{0.5})Co_5$ ribbon is predominantly composed of $(Y-Sm)Co_5$ with a minor amount of Sm_2Co_7 . The presence of the minor 2:7 phase could be attributed to the segregation of the 1:5 phase during the annealing process. As the annealing temperature increases, the main diffraction peaks gradually sharpen. According to the previous discussion, when the wheel speed is 40 m/s, the ribbon exhibits partial amorphous phase. According to the calculations, after heat treatment at 550 °C, 600 °C, and 650 °C, the crystallinity of the ribbon is 59.1%, 67.8%, and 76.5%, respectively. This indicates that with increasing temperature, the amorphous phase gradually transforms into a crystalline phase.

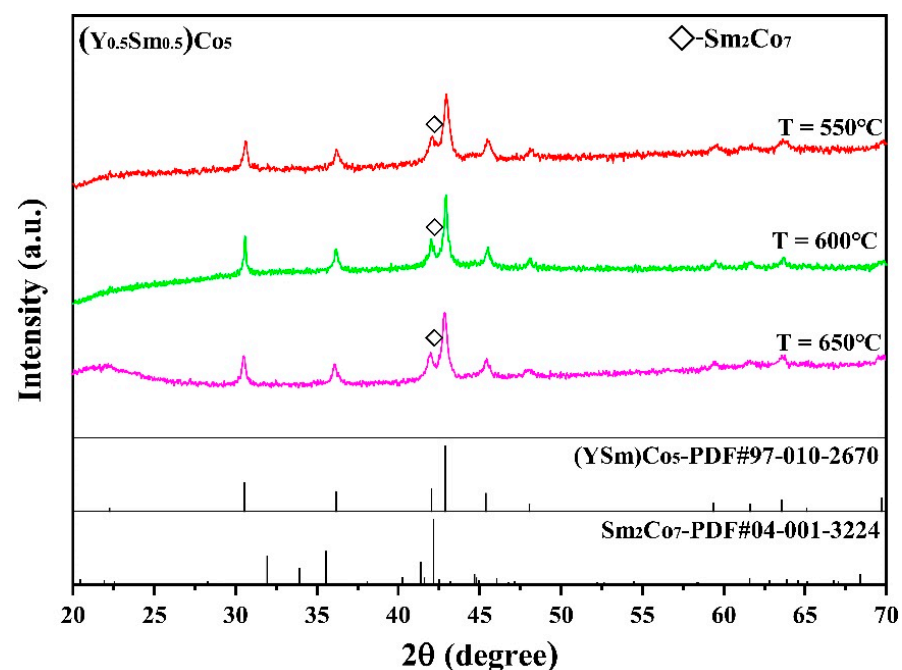


Figure 8. XRD patterns of $(Y_{0.5}Sm_{0.5})Co_5$ ribbon prepared at a wheel speed of 40 m/s after annealed at different temperatures for 30 min.

Figure 9 shows the initial magnetization curves and hysteresis loops (M-H curves) of $(Y_{0.5}Sm_{0.5})Co_5$ melt-spun ribbons annealed at different temperatures for 30 min, prepared with a wheel speed of 40 m/s. Figure 10 illustrates the variations in remanence (B_r), coercivity (H_c), and saturation magnetization (M_s) of the annealed $(Y_{0.5}Sm_{0.5})Co_5$ ribbons with annealing temperature. Corresponding magnetic parameters are provided in Table 2. From Figure 9a, it can be observed that the initial magnetization curve of the $(Y_{0.5}Sm_{0.5})Co_5$ melt-spun ribbon exhibits distinct ferromagnetic characteristics. The initial magnetization intensity of the ribbon rapidly increases with the applied magnetic field, reaching saturation, with the magnetization mechanism regulated by nucleation field. Figure 9b presents the hysteresis loop of the annealed $(Y_{0.5}Sm_{0.5})Co_5$ melt-spun ribbon. In the second quadrant, the demagnetization curve of the ribbon exhibits a relatively smooth profile, indicative of typical single-phase hard magnetic behavior. This observation suggests well-crystallized microstructure within the ribbon. However, there are evident twists in the demagnetization curve, indicating the possible formation of soft magnetic phases (such as Sm_2Co_7) during annealing. The exchange coupling effect between the $(Y-Sm)Co_5$ hard magnetic phase and soft magnetic phase leads to the twists in the demagnetization

curve of the ribbon. From Figure 10 and Table 2, it is revealed that after annealing at 550 °C, both saturation magnetization and remanence of the ribbon increase, showing a certain remanence enhancement effect. The crystallization of the amorphous phase in the ribbon after annealing is the main reason for the improvement in magnetic properties. With increasing annealing temperature, coercivity decreases from 7.98 kOe at 550 °C to 5.17 kOe at 650 °C. This decrease may be attributed to the growth of grain size in the ribbon with increasing annealing temperature, reducing the interaction between grains in the ribbon. Additionally, the increase in annealing temperature promotes the decomposition of the 1:5 phase into 2:7 and 2:17 phases, and the formation of these secondary phases can easily become nucleation centers for antiferromagnetic domains within the 1:5 ribbon, leading to a decrease in coercivity.

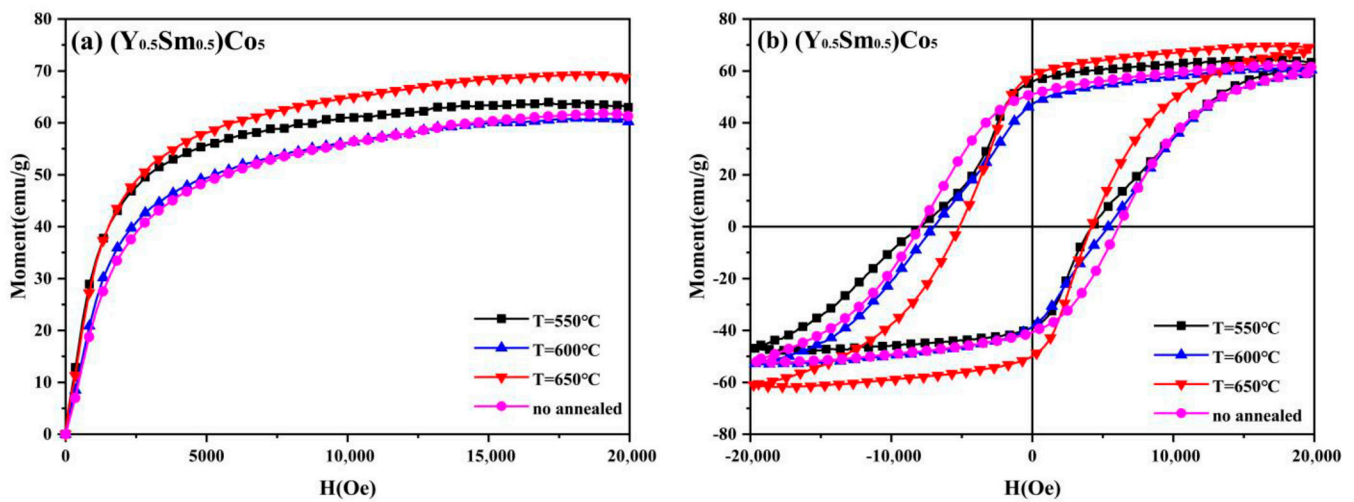


Figure 9. Initial magnetization curves (a) and hysteresis loops (b) of $(Y_{0.5}Sm_{0.5})Co_5$ ribbon annealed at different temperatures.

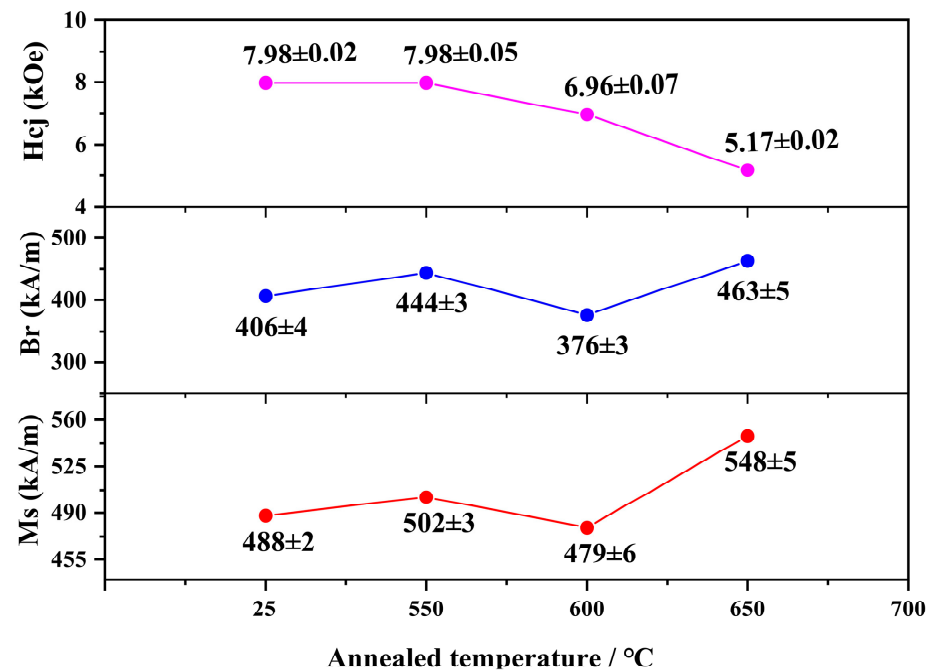


Figure 10. Magnetic properties (H_{cj} , B_r , and M_s) of $(Y_{0.5}Sm_{0.5})Co_5$ ribbon annealed at different temperatures.

In this section, we investigated the phase structure, phase composition, and magnetic properties of $(Y_{0.5}Sm_{0.5})Co_5$ melt-spun ribbons annealed at different temperatures (550 °C, 600 °C, 650 °C) for 30 min. The results reveal that all ribbons were predominantly composed of $(Y-Sm)Co_5$ with small amounts of Sm_2Co_7 . Magnetic measurement results indicated a trend of increasing saturation magnetization and remanence with rising temperature, primarily attributed to the crystallization of the amorphous phase post-annealing. However, the coercivity decreases from 7.98 kOe to 5.17 kOe, attributed to the increase in grain size in the ribbon as annealing temperature rises, reducing the interaction between grains. Additionally, the elevated annealing temperature promotes the decomposition of the 1:5 phase into the 2:7 phase, with the formation of the 2:7 phase serving as easy nucleation sites for antiferromagnetic domains within the 1:5 phase, consequently leading to a decrease in coercivity.

4. Conclusions

This experimental investigation focused on the effects of Sm substitution, wheel speed, and annealing temperature on the phase structure and magnetic properties of $(Y_{1-x}Sm_x)Co_5$ melt-spun ribbons, yielding the following conclusions:

(1) With increasing Sm substitution, X-ray diffraction (XRD) analysis reveals that $(Y_{1-x}Sm_x)Co_5$ ($x = 0.2, 0.3, 0.4, 0.5$) ribbons are composed of $(Y-Sm)Co_5$ with a $CaCu_5$ -type structure and space group $P63/mmc$. Magnetic measurements indicate that the magnetization mechanism is regulated by the nucleation field. As the Sm substitution increases, the proportion of $tSmCo_5$ increases, leading to a decrease in saturation magnetization from 726 kA/m to 488 kA/m and remanence from 479 kA/m to 406 kA/m, while coercivity increased from 0.79 to 7.98 kOe.

(2) Based on the XRD results, the $(Y_{0.5}Sm_{0.5})Co_5$ ribbon prepared at wheel speeds of 20 m/s and 40 m/s are composed of $(Y-Sm)_2Co_{17}$, while the ribbon at a wheel speed of 30 m/s is composed of $(Y-Sm)Co_5$ and Sm_2Co_7 . The magnetic measurements show that the coercivity (H_c), the remanence (B_r), and the saturation magnetization (M_s) of the $(Y_{0.5}Sm_{0.5})Co_5$ ribbon increase gradually with the increase in wheel speed. The variation in magnetic properties is primarily attributed to the formation of nucleation centers for reversed magnetic domain (2:7 and 2:17 phases). At a wheel speed of 40 m/s, the ribbon is primarily composed of a single-phase $(Y-Sm)Co_5$, exhibiting excellent magnetic properties under optimal conditions (coercivity of 7.98 kOe, remanence of 406 kA/m, saturation magnetization of 488 kA/m).

(3) The $(Y_{0.5}Sm_{0.5})Co_5$ ribbon prepared at a wheel speed of 40 m/s consists of $(Y-Sm)Co_5$ and a small amount of Sm_2Co_7 according to the XRD results after annealing at 550 °C, 600 °C, and 650 °C for 30 min. The optimization of the annealing process promotes the crystallization of the amorphous phase. The best magnetic performance was achieved at an annealing temperature of 550 °C, resulting in a coercivity of 7.98 kOe, remanence of 444 kA/m, and saturation magnetization intensity of 508 kA/m.

Author Contributions: Conceptualization, X.L., S.Y., Q.Y. and J.W.; methodology, X.L., X.Z., F.D. and J.W.; software, X.Z. and F.D.; validation, X.L., X.Z. and F.D.; formal analysis, X.L., Q.Y. and J.W.; investigation, J.W. and Q.Y.; resources, Q.Y. and J.W.; data curation, X.L., X.Z. and S.Y.; writing—original draft preparation, X.L., S.Y., Q.Y. and J.W.; writing—review and editing, X.L., S.Y., Q.Y. and J.W.; visualization, X.Z.; supervision, Q.Y. and J.W.; project administration, J.W. and Q.Y.; funding acquisition, Q.Y. and J.W. All authors have read and agreed to the published version of the manuscript.

Funding: This work was supported financially by Guangxi Natural Science Foundation (2020GXNSFFA297004), the National Natural Science Foundation of China (51971069), and the Engineering Research Center of Electronic Information Materials and Devices (EIMD-AA202004), Guilin University of Electronic Technology, China.

Data Availability Statement: The original contributions presented in the study are included in the article, further inquiries can be directed to the corresponding author.

Conflicts of Interest: The authors declare no conflicts of interest.

References

1. Chen, R.J.; Xia, X.S.; Tang, X.; Yan, A. Significant Progress for Hot-Deformed Nd-Fe-B Magnets: A Review. *Materials* **2023**, *16*, 4789. [[CrossRef](#)] [[PubMed](#)]
2. Liu, Z.W.; He, J.Y.; Ramanujan, R.V. Significant progress of grain boundary diffusion process for cost-effective rare earth permanent magnets: A review. *Mater. Des.* **2021**, *209*, 110004. [[CrossRef](#)]
3. Coey, J.M.D. Perspective and Prospects for Rare Earth Permanent Magnets. *J. Eng.* **2020**, *6*, 119–131. [[CrossRef](#)]
4. Mishra, A.; Khoshsima, S.; Tomse, T.; Podmiljsak, B.; Sturm, S.; Burkhardt, C.; Zuzek, K. Short-Loop Recycling of Nd-Fe-B Permanent Magnets: A Sustainable Solution for the RE₂Fe₁₄B Matrix Phase Recovery. *Materials* **2023**, *16*, 6565. [[CrossRef](#)]
5. Ming, X.; Han, X.; Wang, J.H.; Wang, L.C.; Xiong, J.F.; Liu, D.; Yan, G.L.; Shen, B.G. Comprehensively improved magnetic performance of Nd-Fe-B magnets with high-efficiency grain boundary diffusion of heavy rare earth. *Vacuum* **2024**, *222*, 113003. [[CrossRef](#)]
6. Liu, Z.W.; He, J.Y.; Zhou, Q.; Huang, Y.L.; Jiang, Q.Z. Development of non-rare earth grain boundary modification techniques for Nd-Fe-B permanent magnets. *J. Mar. Sci. Technol.* **2022**, *98*, 51–61. [[CrossRef](#)]
7. Hono, K.; Sepehri-Amin, H. Strategy for high-coercivity Nd-Fe-B magnets. *Scr. Mater.* **2012**, *67*, 530–535. [[CrossRef](#)]
8. Hioki, K. Development of High-Performance Hot-Deformed Neodymium-Iron-Boron Magnets without Heavy Rare-Earth Elements. *Materials* **2023**, *16*, 6581. [[CrossRef](#)] [[PubMed](#)]
9. Guo, K.; Lu, H.; Xu, G.J.; Liu, D.; Wang, H.B.; Liu, X.M.; Song, X.Y. Recent progress in nanocrystalline Sm-Co based magnets. *Mater. Today Chem.* **2022**, *25*, 100983. [[CrossRef](#)]
10. Park, K.; Hirayama, Y.; Wang, J.; Kobashi, M. Ultra-high coercivity Sm-Co bulk magnets with remarkable thermal stability. *Scr. Mater.* **2022**, *218*, 114847. [[CrossRef](#)]
11. Teng, Y.; Li, Y.Q.; Liu, W.Q.; Xu, X.C.; Wang, Z.J.; Yang, J.J.; Zhang, D.T.; Zhang, H.G.; Lu, Q.M.; Wu, Q.; et al. Coercivity mechanism of high-performance anisotropic heterostructure SmCo₅ magnets. *J. Rare Earths* **2023**. [[CrossRef](#)]
12. Li, Y.Q.; Teng, Y.; Wang, M.K.; Zhang, D.T.; Lu, Q.M.; Liu, W.Q.; Xia, W.X.; Yue, M. Analysis on the inhomogeneous magnetization reversal in the sintered Sm-Co magnet. *J. Magn. Magn. Mater.* **2023**, *571*, 170468. [[CrossRef](#)]
13. Li, L.Y.; Gao, Z.; Ge, Y.C.; Yan, A.; Zhang, W.; Peng, Y.D. Anisotropic nanocrystalline SmCo_{4.8}Cr_{0.12}C_{0.08} permanent magnets fabricated using melt-spinning method. *J. Alloys Compd.* **2017**, *714*, 194–197. [[CrossRef](#)]
14. Su, Y.F.; Su, H.; Zhu, Y.J.; Wang, F.; Du, J.; Xia, W.X.; Yan, A.; Liu, J.P.; Zhang, J. Effects of magnetic field heat treatment on Sm-Co/a-Fe nanocomposite permanent magnetic materials prepared by high energy ball milling. *J. Alloys Compd.* **2015**, *647*, 375–379. [[CrossRef](#)]
15. Gabay, A.M.; Hu, X.C.; Hadjipanayis, G.C. Preparation of YCo₅, PrCo₅ and SmCo₅ anisotropic high-coercivity powders via mechanochemistry. *J. Magn. Magn. Mater.* **2014**, *368*, 75–81. [[CrossRef](#)]
16. Chang, H.W.; Guo, Y.M.; Liao, S.H.; Chang, W.C.; Shaw, C.C. Magnetic property improvement of melt spun LaCo₅-based nanocomposites with Y, Fe and C substitutions. *J. Alloys Compd.* **2020**, *821*, 153271. [[CrossRef](#)]
17. Asali, A.; Fidler, J.; Suess, D. Influence of changes in electronic structure on magnetocrystalline anisotropy of YCo₅ and related compounds. *J. Magn. Magn. Mater.* **2019**, *485*, 61–68. [[CrossRef](#)]
18. Sharma, S.; Hildebrandt, E.; Major, M.; Komissinskiy, P.; Radulov, I.; Alff, L. CeCo₅ thin films with perpendicular anisotropy grown by molecular beam epitaxy. *J. Magn. Magn. Mater.* **2018**, *452*, 80–85. [[CrossRef](#)]
19. Sharma, S.; Hildebrandt, E.; Sharath, S.U.; Radulov, I.; Alff, L. YCo_{5±x} thin films with perpendicular anisotropy grown by molecular beam epitaxy. *J. Magn. Magn. Mater.* **2017**, *432*, 382–386. [[CrossRef](#)]
20. Passos, F.; Cornejo, D.; Fantini, M.; Nilsen, G.; Martelli, V.; Jiménez, J.L. Magnetic, electronic, and structural investigation of the strongly correlated Y_{1-x}Sm_xCo₅ system. *SciPost Phys. Proc.* **2023**, *11*, 211–218.
21. Okumura, H.; Fukushima, T.; Akai, H.; Ogura, M. First-principles calculation of magnetocrystalline anisotropy of Y(Co,Fe,Ni,Cu)₅ based on full-potential KKR Green's function method. *Solid. State. Commun.* **2023**, *373–374*, 115257. [[CrossRef](#)]
22. Gjoka, M.; Sempros, G.; Giaremis, S.; Kioseoglou, J.; Sarafidis, C. On Structural and Magnetic Properties of Substituted SmCo₅ Materials. *Materials* **2023**, *16*, 547. [[CrossRef](#)] [[PubMed](#)]
23. Gjoka, M.; Sarafidis, C.; Giaremis, S. Towards Production of Cost-Effective Modification of SmCo₅-Type Alloys Suitable for Permanent Magnets. *Materials* **2024**, *17*, 808. [[CrossRef](#)] [[PubMed](#)]
24. Chouhan, R.K.; Pathak, A.K.; Paudyal, D. Understanding the origin of magneto-crystalline anisotropy in pure and Fe/Si substituted SmCo₅. *J. Magn. Magn. Mater.* **2021**, *522*, 167549. [[CrossRef](#)]
25. Larson, P.; Mazin, I.I.; Papaconstantopoulos, D.A. Effects of doping on the magnetic anisotropy energy in SmCo_{5-x}Fe_x and YCo_{5-x}Fe_x. *Phys. Rev. B* **2004**, *69*, 134408. [[CrossRef](#)]
26. Staab, F.; Yang, Y.Y.W.; Foya, E.; Bruder, E.; Zingsem, B.; Adabifiroozjaei, E.; Nasiou, D.; Skokov, K.; Koch, D.; Farle, M.; et al. Influence of amorphous phase on coercivity in SmCo₅-Cu nanocomposites. *Scr. Mater.* **2024**, *240*, 115808. [[CrossRef](#)]
27. Tang, W.; Zhang, Y.; Hadjipanayis, G.C. Effect of Zr on the microstructure and magnetic properties of Sm(Co_{bal}Fe_{0.1}Cu_{0.088}Zr_x)_{8.5} magnets. *J. Appl. Phys.* **2000**, *87*, 399–403. [[CrossRef](#)]
28. Yao, Z.; Qi, X.; Jiang, C.B. Structural and magnetic properties of SmCo_{5.6}Ti_{0.4} alloy. *J. Magn. Magn. Mater.* **2008**, *320*, 1717–1721. [[CrossRef](#)]

29. Patrick, C.E.; Kumar, S.; Balakrishnan, G.; Edwards, R.S.; Lees, M.R.; Mendive-Tapia, E.; Petit, L.; Staunton, J.B. Rare-earth/transition-metal magnetic interactions in pristine and (Ni,Fe)-doped YCo₅ and GdCo₅. *Phys. Rev. Mater.* **2017**, *1*, 024411. [[CrossRef](#)]
30. Chang, H.; Rao, G.; Liang, J.; Guo, Y.; Liu, S.; Du, H. Influence of exotic Mn on magnetic properties of YCo_{5.0-x}Mn_xGa_{7.0} (0.05 ≤ x ≤ 3.0). *Appl. Phys. A-Mater.* **2005**, *81*, 1309–1312. [[CrossRef](#)]
31. Chang, H.W.; Ou, W.C.; Lee, Y.I.; Shih, C.W.; Chang, W.C.; Yang, C.C.; Shaw, C.C. Magnetic properties and microstructure of melt spun YCo_{5-x}M_x ribbons (M=C and Sn; x=0-0.3). *J. Alloys Compd.* **2018**, *747*, 236–241. [[CrossRef](#)]
32. Radakovic, J.; Batalovic, K.; Umicevic, A.; Miletic, G.I. Theoretical investigation of interaction of hydrogen and intermetallic compound YCo₅. *J. Alloys Compd.* **2017**, *726*, 1085–1091. [[CrossRef](#)]
33. Isnard, O.; Arnold, Z.; Coroian, N.; Kamarad, J. Volume effect in magnetic properties of the YCo₄Si compound. *J. Magn. Magn. Mater.* **2007**, *316*, 325–327. [[CrossRef](#)]
34. Chen, J.C.; Wang, F.Q.; Wang, F.; Meng, F.B.; Zhang, J. Phase structure and magnetic properties of La/Ce substituted nanocomposite SmCo₅/α-Fe magnets prepared by high energy ball milling and subsequent annealing. *J. Magn. Magn. Mater.* **2021**, *521*, 167534. [[CrossRef](#)]
35. Yang, J.J.; Zhang, D.T.; Zhu, R.C.; Xu, X.C.; Wu, D.; Li, Y.Q.; Liu, W.Q.; Yue, M. Effect of (Sm,Pr)₂Co₇ phase on magnetic properties of high-performance (Sm,Pr)Co₅ magnet based on EBSD analysis and magnetic domain observation. *Mater. Charact.* **2021**, *181*, 111478. [[CrossRef](#)]
36. Jin, H.M.; Zhao, T.S.; Yan, Y.; Han, X.F. Abnormal magnetic properties of the Nd ion in Nd_xY_{1-x}Co₅ compounds. *Solid State Commun.* **1992**, *82*, 915–918.
37. Banerjee, D.; Suresh, K.G.; Nigam, A.K. Effect of Y substitution on the structural and magnetic properties of Dy_{1-x}Y_xCo₅ compounds. *J. Magn. Magn. Mater.* **2008**, *320*, 374–378. [[CrossRef](#)]
38. Zuo, J.H.; Yue, M.; Wang, Y.Q.; Lu, Q.M.; Liu, Y.Q.; Zhang, D.T.; Liu, W.Q.; Zhang, J.X.; Guo, Z.H.; Li, W. Influence of Tm on crystal structure and magnetic properties of SmCo₅ compounds. *Rare. Met. Mater. Eng.* **2015**, *44*, 0834–0837.
39. Hidalgo-Gonzalez, J.L.; Rivera Gomez, F.J.; Matutes-Aquino, J.A. Nanocrystalline Y_{0.5}Sm_{0.5}Co₅ ribbons obtained by melt spinning. *J. Appl. Phys.* **2009**, *105*, 07A748. [[CrossRef](#)]
40. Khan, Y.; Feldmann, D. Crystal structure of SmCo₅. *J. Less-Common. Met.* **1973**, *31*, 211–220. [[CrossRef](#)]
41. Wernick, J.H.; Geller, S. Transition element-rare earth compounds with Cu₅Ca. *Acta Chromatogr.* **1959**, *12*, 662–665. [[CrossRef](#)]
42. Duerrschnebe, M.; Yi, M.; Uestuener, K.; Liesegang, M.; Katter, M.; Kleebe, H.-J.; Xu, B.; Gutfleisch, O.; Molina-Luna, L. Atomic structure and domain wall pinning in samarium-cobalt-based permanent magnets. *Nat. Commun.* **2017**, *8*, 54. [[CrossRef](#)]
43. Yan, A.R.; Zhang, W.Y.; Zhang, H.W.; Shen, B.G. Melt-spun magnetically anisotropic SmCo₅ ribbons with high permanent performance. *J. Magn. Magn. Mater.* **2000**, *210*, L10–L14. [[CrossRef](#)]
44. Elizalde, J.T.; Matutes, J.A.; Davies, H.A.; Liu, Z. Magnetic and structural study of melt-spun YCo₅ ribbons. *J. Magn. Magn. Mater.* **2005**, *294*, e137–e140. [[CrossRef](#)]
45. Liu, X.; Wang, J.; Yang, S.Y.; Zheng, X.P.; Yao, Q.R.; Du, Y.S.; Zhang, L.G.; Rao, G.H.; Zhou, H.Y. Experimental determination of phase equilibria in the Y-Co-Ti ternary system through diffusion couples and equilibrium alloys. *Calphad* **2023**, *81*, 102551. [[CrossRef](#)]
46. Liu, P.P.; Dai, F.L.; Luo, L.; Chen, D.K.; Yao, Q.R.; Wang, J.; Rao, G.H.; Zhou, H.Y. Experimental study and thermodynamic calculation of the Sm-Co-Fe system. *Calphad* **2022**, *78*, 102447. [[CrossRef](#)]

Disclaimer/Publisher’s Note: The statements, opinions and data contained in all publications are solely those of the individual author(s) and contributor(s) and not of MDPI and/or the editor(s). MDPI and/or the editor(s) disclaim responsibility for any injury to people or property resulting from any ideas, methods, instructions or products referred to in the content.